Contents lists available at ScienceDirect

Planetary and Space Science

Stereo topographic models of Mercury after three MESSENGER flybys

Frank Preusker [a,*], Jürgen Oberst [a], James W. Head [b], Thomas R. Watters [c], Mark S. Robinson [d], Maria T. Zuber [e], Sean C. Solomon [f]

[a] German Aerospace Center (DLR), Rutherfordstr. 2, Institute of Planetary Research, D-12489 Berlin, Germany
[b] Department of Geological Sciences, Brown University, Providence, RI 02912, USA
[c] Center for Earth and Planetary Studies, National Air and Space Museum, Smithsonian Institution, Washington, DC 20560, USA
[d] School of Earth and Space Exploration, Arizona State University, Tempe, AZ 85287, USA
[e] Department of Earth, Atmospheric, and Planetary Sciences, Massachusetts Institute of Technology, Cambridge, MA 02139-4307, USA
[f] Department of Terrestrial Magnetism, Carnegie Institution of Washington, Washington, DC 20015, USA.

ARTICLE INFO

ABSTRACT

From photogrammetric analysis of stereo images of Mercury obtained during three MESSENGER flybys, we have produced three digital terrain models (DTMs) that have a grid spacing of 1 km and together cover 30% of the planet's surface. The terrain models provide a rich source of information on the morphology of Mercury's surface, including details of tectonic scarp systems as well as impact craters and basins. More than 400 craters larger than 15 km in diameter are included in the models. Additionally, the models provide important test cases for the analysis of stereo image data to be collected during MESSENGER's orbital mission phase. Small lateral offsets and differences in trends between stereo DTMs and laser altimeter profiles may be due to remaining errors in spacecraft position, instrument pointing, or Mercury coordinate knowledge. Such errors should be resolved during the orbital mission phase, when more joint analyses of data and detailed orbit modeling will be possible.

© 2011 Elsevier Ltd. All rights reserved.

1. Introduction

Mercury is the smallest and the least explored of all the terrestrial planets. Considerable information on a planet's history and on the processes that have acted on its surface can be obtained from the studies of the planet's surface morphology. Until recently, however, only limited information was available for Mercury. Stereo images collected by the Mariner 10 spacecraft during flybys of Mercury in 1974–1975 have been used to reconstruct maps of surface topography (Cook and Robinson, 2000; Watters et al., 2001). These maps, however, suffered from difficulties in the radiometric and geometric calibration of the Mariner 10 vidicon sensors. Moreover, stereo coverage was restricted to portions of the southern hemisphere (~20% of the planet's surface). Topographic data have also been obtained from Earth-based radar delay and Doppler data (Slade et al., 1997), but only along linear profiles in equatorial areas and with limited spatial resolution (approximately 5 km in longitude and 100 km in latitude).

The MErcury Surface, Space ENvironment, GEochemistry, and Ranging (MESSENGER) spacecraft is only the second probe to visit the innermost planet. The spacecraft is equipped with a well-calibrated imaging system (Hawkins et al., 2007, 2009), and data obtained during three Mercury flybys in 2008–2009 (Solomon et al., 2008) included images that allowed stereo topographic reconstructions for a substantial portion of the planet not covered by Mariner 10. The stereo analysis in this paper constitutes an important test case for MESSENGER's orbital mission phase, to begin in March 2011, when dedicated stereo mapping sequences will be obtained at near-global coverage.

2. Data

2.1. Camera system

MESSENGER's Mercury Dual Imaging System (MDIS) consists of two framing cameras, a wide-angle camera (WAC) and a narrow-angle camera (NAC), co-aligned on a pivot platform and equipped with identical 1024×1024-pixel charge-coupled device (CCD) sensors (Hawkins et al., 2007). NAC, the principal tool for stereo analysis in this paper, consists of a compact off-axis optical system that has been geometrically calibrated using laboratory as well as in-flight stellar observations (Hawkins et al., 2007, 2009). Image mosaics are obtained by a combination of pivot platform movement and spacecraft motion.
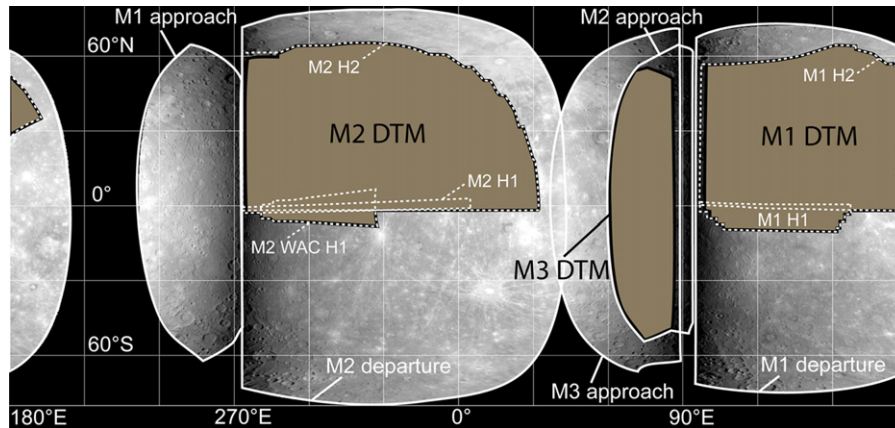
Fig. 1. Locations of MESSENGER image mosaics (Table 1) (outlined in white) and MESSENGER digital terrain models (brown shading) discussed in this paper, overlaid on a global MDIS image mosaic in cylindrical projection.

Table 1
Overview of digital terrain models.

DTM	Image mosaics	Image scale (m)	Image count	Object point count (10^6)	3D point precision (m)
–	M1 approach	520–580	38	–	–
M1 DTM	M1 H1	120–180	68	150.0	250
	M1 H2	300–400	93		
	M1 departure	500–600	47		
M2 DTM	M2 WAC H1	250–750	5	220.0	290
	M2 H1	100–300	35		
	M2 H2	250–350	173		
	M2 departure	500–650	47		
M3 DTM	M2 approach	500–550	20	34.5	160
	M3 approach	450–500	28		

2.2. Stereo image coverage

The pivot-based scanning capability of MDIS allowed acquisition of several contiguous image mosaics (Fig. 1) during MESSEN-GER's three Mercury flybys on 14 January 2008 (M1), 6 October 2008 (M2), and 29 September 2009 (M3). These mosaics were constructed from a total of 2163 images, approximately 660 of which had a mean image resolution better than 550 m. The images were assembled into 10 individual sub-mosaics (Table 1). Five full-hemisphere sub-mosaics, M1 approach, M1 departure, M2 approach, M2 departure, and M3 approach, cover ~80% of Mercury's surface. In addition, MESSENGER acquired images from which five high-resolution local image mosaics were constructed: M1 H1, M1 H2, M2 H1, M2 H2, and M2 WAC H1 (Fig. 1).

From the images collected during the three flybys, there are three separate areas covered stereoscopically (Fig. 1) by a total of 516 images (Table 1). The stereo mosaics were taken under similar illumination conditions but variable viewing conditions (e.g., Fig. 2a). Apart from images viewed nearly at nadir, large areas in these mosaics were located near the planetary limbs, where emission angles (measured from the local vertical) were as great as 80° (Fig. 2a).

Stereo angle is an even more important parameter than emission angle for the generation of a high-fidelity digital terrain model (DTM). Stereo angles were appropriate for the M1 H1, M2 H1, M2 WAC H1, and M3 DTMs (up to 40° and 20–30°), but for the M1 H2 and M2 H2 mosaics stereo angles were often less than 14°, and the stereo angle was only 4° in the southwestern part of M1 H2, as may be seen in Fig. 2b. Maps of the relative three-dimensional (3D)

precision achieved in the DTMs (Figs. 2c and 3) reflect a high sensitivity to stereo geometry. Even small residual errors within the radial distortion model are visible in the form of a decrease of the relative 3D precision toward the edges of the stereo models M1 H2 and M2 H2. In contrast, such effects are nearly unresolvable within the M1 H1, M2 H1, M2 WAC H1, and M3 DTMs. Visual inspection of the final DTMs indicates that with the additional redundancy provided by the typical multiple overlap (more than two images) at the image edges, an increase of the nominal 3D forward ray-intersection error does not necessarily lead to a marked decrease of the quality of the heights within these DTMs.

3. Photogrammetric stereo image analysis

The photogrammetric stereo analysis is based on algorithms and software realizations used extensively on previous planetary image data sets (Giese et al., 1998, 2006; Gwinner et al., 2009, 2010). The processing involves several stages and includes pointing corrections made with photogrammetric block-adjustment techniques, multi-image matching, and the generation of DTMs and orthoimage mosaics.

3.1. Block adjustments

Beginning with the nominal spacecraft position and camera pointing data provided by the MESSENGER project, image footprint information was generated to identify areas of stereo overlap between images. Next, multi-image matching was applied to all image data in overlapping areas to derive conjugate points (commonly termed tie points). A large matching grid size was used to avoid excessive numbers of points (Table 2).

The resulting image coordinates of the tie points and the nominal navigation data (pointing and position) for each image form the input (observations) to photogrammetric block adjustment. The ground coordinates and the orientation of each image were considered as unknowns. In contrast, the nominal spacecraft positions and camera pointing were assumed to be correct within the random errors assumed to be ±50 m and ±1.0 mrad, respectively (E.J. Finnegan and F.S. Turner, pers. comm., 2010). We expect that any systematic offsets of the spacecraft trajectory from nominal will not affect the characteristics of the terrain modeling beyond overall positioning. We estimate that the accuracy of the measured image coordinates was ±0.3 pixel. Only tie points that concatenated at least three images were selected to minimize the total number of tie points and provide
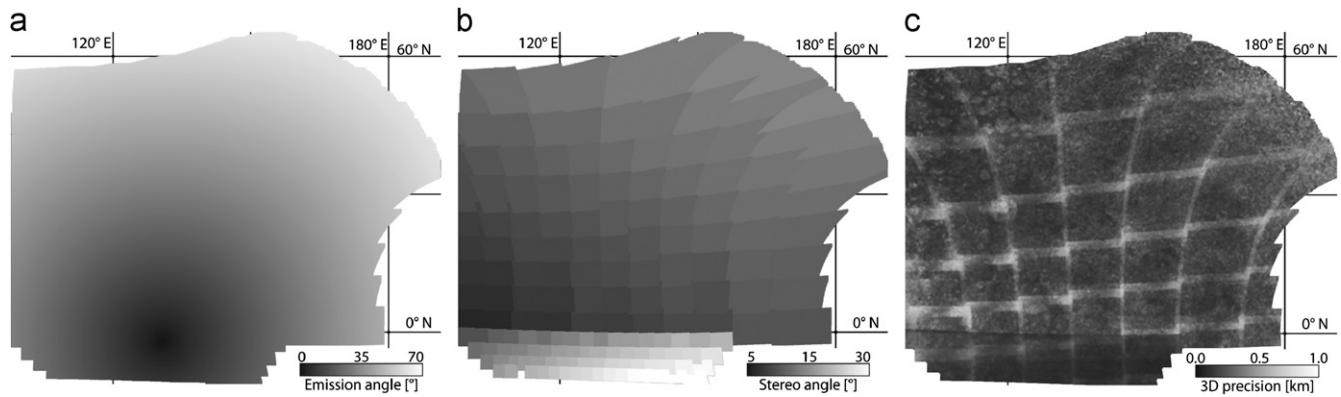
Fig. 2. (a) Graphical depiction of emission angles for images in the M1 departure mosaic, which was used to compute the M1 DTM. (b) Stereo convergence angles between the M1 departure mosaic and the two mosaics M1 H1 and M1 H2, all of which were used to compute the M1 DTM. (c) Three-dimensional (3D) point accuracies for the M1 DTM. The largest point errors (approximately 500 m) are well below the DTM grid size.
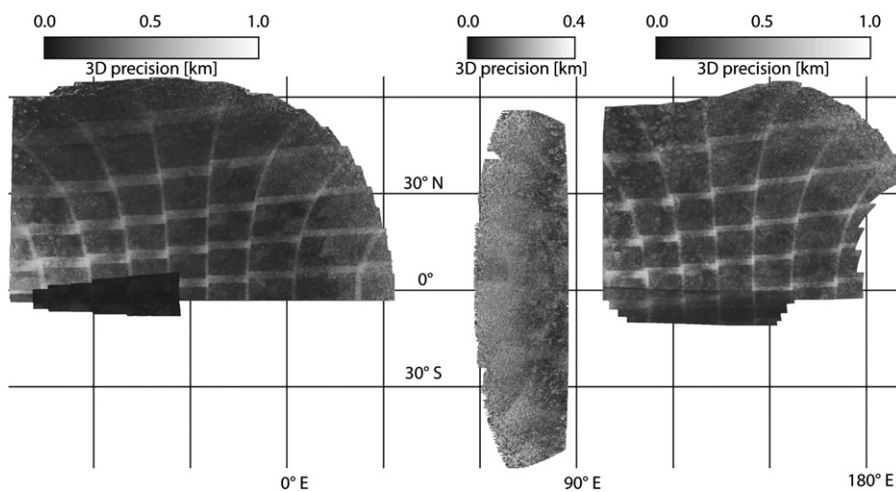

Fig. 3. Three-dimensional point accuracies for the three DTMs, for comparison with Fig. 2c. Note the relatively small errors for M3 DTM.

Table 2
Block adjustment results.

Block	Image count	Tie-point count	Control-point accuracy (m)	
			Before	After
M1 block	208	~12000	~6300	220
M2 block	260	~15000	~5100	265
M3 block	48	~5600	~2000	145

stability to the adjustment solution for each block. As a result of the block adjustment, we obtained improved orientation data, which were used in all further processing described in this paper.

3.2. Image matching

The images were pre-rectified on a reference sphere with a radius of 2440 km using the improved orientation data, as described above. A multi-image matching technique was applied to derive tie points between images that form stereo observations. The pre-rectification warrants that the search for tie points be limited to small areas. Hence, point misidentifications and gaps were reduced to a minimum. The matching algorithm is an area-based image correlation to derive approximate values for the match-point coordinates, which are refined to sub-pixel accuracy by least-squares matching (Wewel, 1996). After the matching, the derived image coordinates (which refer to pre-rectified images) were transformed back to the geometry of the raw images, using the history files generated during the pre-rectification. The accuracy of this back-transformation is better than 0.1 pixel (Scholten et al., 2005).

3.3. DTM generation

Beginning with the large numbers of coordinate pairs for the matched points, the geometric calibration and improved orientation data were used to compute object point coordinates by means of forward ray intersection. Here, least-squares adjustment was applied for this over-determined problem. As a result, we obtained object point coordinates and their relative accuracy in Mercury body-fixed Cartesian coordinates.

For the generation of a gridded DTM, the object points from the different stereo models were merged. The object points were first transformed from Mercury body-fixed Cartesian coordinates to geographic latitude/longitude/height and then transformed to chosen map projections (simple cylindrical equidistant). A pixel scale of 1 km was chosen. Object points located within a DTM pixel were averaged using neighborhood statistics (Gwinner et al., 2010). For regions that lack any object-point information, a gap-filling algorithm using DTM pyramids with reduced resolution was applied.

3.4. True orthoimage mosaics

Images were resampled to derive orthoimage mosaics. From the topography models, each image pixel was referenced to latitude and longitude using ray intersection points with the terrain model. These true orthoimages are thus free of parallax errors and suited for the production of geometrically correct image mosaics, as needed for further analysis, e.g., for comparison with laser altimetry (see below).

4. Digital terrain models

4.1. M1 DTM

The M1 DTM was derived from 208 stereo images acquired during the first flyby. The images were combined into three individual sub-mosaics (Table 1). In total 241 individual matching runs were carried out on at least double- or triple-overlapping images to yield 150 million object points with a mean intersection error of ± 250 m. The M1 DTM covers 12% (8.8×10^6 km^2) of Mercury's surface (Fig. 4) and includes the Caloris impact basin (1550 km diameter). The coverage of the model is increased towards the limb over what was reported previously (Oberst et al., 2010). Large portions of the DTM show topographic fabric consisting of relatively narrow, positive- and negative-relief landforms oriented radial to Caloris, most prominently expressed to the southwest and east-northeast of the basin (see arrows on figure). In addition, the DTM features a large and complex fault system near Beagle Rupes, one of the largest lobate scarps seen on Mercury (Watters et al., 2009a).

4.2. M2 DTM

The M2 DTM, the largest among the three DTMs, was derived from 260 stereo images acquired during the second flyby and includes four sub-mosaics (Table 1, Fig. 5). 220 million object points with a mean intersection error of ± 290 m were computed from 226 individual matching runs. The M2 DTM covers 15% (11.3×10^6 km^2) of Mercury's surface and is limited by the

Fig. 5. M2 DTM (hill-shaded, color-coded). The black arrow indicates the location of a newly recognized, unnamed basin, and white arrows denote the locations of possible degraded impact basins.

positions of the limb and the terminator (at the time of M2) to the east and west, respectively. The DTM covers mostly heavily cratered terrain, in contrast to the M1 DTM. A large ($\sim$800-km-diameter) unnamed impact basin (centered at 16.4°N, 19.6°E), not evident in the corresponding images because of low incidence angles (measured from the local vertical), is a prominent feature in the DTM. Several more highly degraded basins are visible in DTM. Like the M1 DTM, this second DTM also shows a number of high-relief fault structures, some extending over distances of up to several hundred kilometers (Fig. 5).

4.3. M3 DTM

Finally, the M3 DTM was produced from a combination of the two approach mosaics constructed from images acquired during the second and third flybys. Owing to favorable stereo geometry with stereo angles of $\sim$25°, the geometric accuracy of this DTM is the best among the three (Fig. 3). However, because the two mosaics were taken at different local times, i.e., different illuminations, the stereo matching is subject to error in regions with shadows. In total 48 stereo images were used to compute 34.5 million object points with a mean intersection error as small as ± 160 m. This smallest among the three DTMs is elongated, extending from high northern to high southern latitudes, and covers $\sim$5% (4.5×10^6 km^2) of Mercury's surface. Prominent in this DTM is the Rembrandt impact basin, approximately half of which is covered by the terrain model (Fig. 6). The DTM also includes several prominent lobate scarps in the southern hemisphere, including the longest scarp yet found on Mercury that crosscuts the Rembrandt basin (Watters et al., 2009b).

4.4. Some general attributes

All DTMs were produced with a common grid spacing of 1 km, a value chosen to yield $\sim$15 object points per DTM pixel on average. The three separate DTMs were merged to a single global DTM (Fig. 7), which covers approximately one third of Mercury's surface. Although the DTMs were generated separately, average heights and topographic trends appear consistent. The total range of height over all DTMs is approximately 9.5 km (-4.5 to 5 km relative to the planetary datum). The average DTM height is 260 m, implying an average planetary radius for the regions of these DTMs of 2440.3 km. (An ellipsoid oriented to match Mercury's principal coordinate axes and fit to these terrain models has semi-major axes $a=2441.1$ km, $b=2439.8$ km, and $c=2439.6$ km, with a and b constrained to lie within Mercury's equatorial plane and c along the spin axis). The terrain models
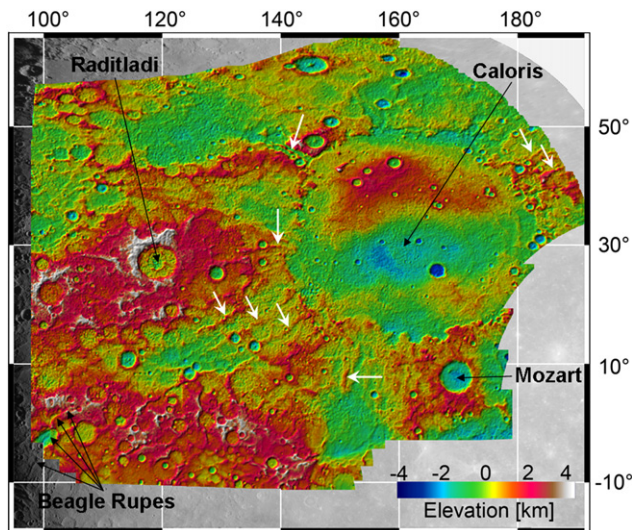

Fig. 4. M1 DTM (hill-shaded, color-coded). Heights are given with respect to a sphere of radius 2440 km. Several notable features are indicated with black arrows. White arrows denote examples of topographic fabric radial to the Caloris impact basin.
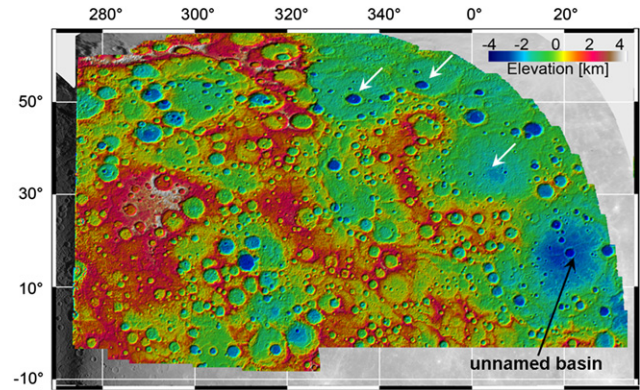
feature large numbers of impact craters that span a range of sizes and degradation states. We estimate that a total of ~400 craters larger than 15 km in diameter are included in these three models.
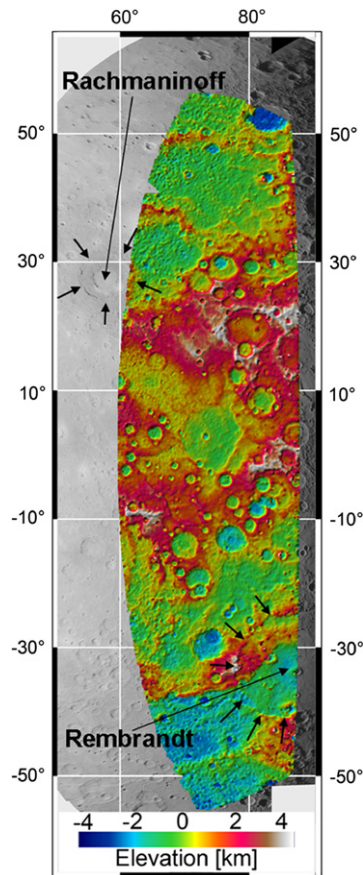

Fig. 6. M3 DTM (hill-shaded, color-coded). Arrows point to the western half of the rim of the Rembrandt impact basin and to the Rachmaninoff basin.

5. Comparison with laser altimetry

Portions of the Mercury Laser Altimeter (MLA) profiles obtained during MESSENGER's first and second Mercury flybys (Zuber et al., 2008; Smith et al., 2010) cross into the areas of the M2 and M3 DTMs. This overlap provides the opportunity to compare the two data sets and in particular to identify their possible relative offsets and differences in long-wavelength trends. Using the high-spatial-resolution and accurate MLA data as a reference, we can also study the effective resolution of the stereo DTMs (Fig. 7).

The MLA profiles obtained during M1 and M2 are both near Mercury's equatorial plane, but on opposite sides of the planet. The laser footprint on the surface varied between 20 and 150 m in diameter along the profiles, in proportion to the height of the spacecraft given the ~80 μrad divergence of the laser beam at $1/e^2$ power. The spacing between shots along the ground track was approximately 700 and 600 m for M1 and M2, respectively. MLA profile tracks were plotted on the orthomosaics using the nominal footprint centers of the laser provided by the MLA team (Figs. 8–10). The DTM height profiles were extracted from the DTM along the MLA ground tracks.

5.1. M2 DTM vs. MLA profile from M1

There is only a small region of overlap between the M2 DTM and the MLA profile obtained during M1. This overlap occurs near the southern edge of the terrain model from 14° to 22°E longitude. In total, 231 MLA shots over a distance of 718 km (corresponding to a mean shot spacing of 3.1 km) provide the overlap. MLA was operated off-nadir (by ~58°) for this part of the track. The comparison between the MLA results and DTM indicates an average height offset of 420 m (Fig. 8).

5.2. M2 DTM vs. MLA profile from M2

The overlap of the M2 DTM and the portion of the MLA profile obtained during M2 from 274° to 286°E longitude is also confined to a small region. In total 221 valid shots were obtained, spread
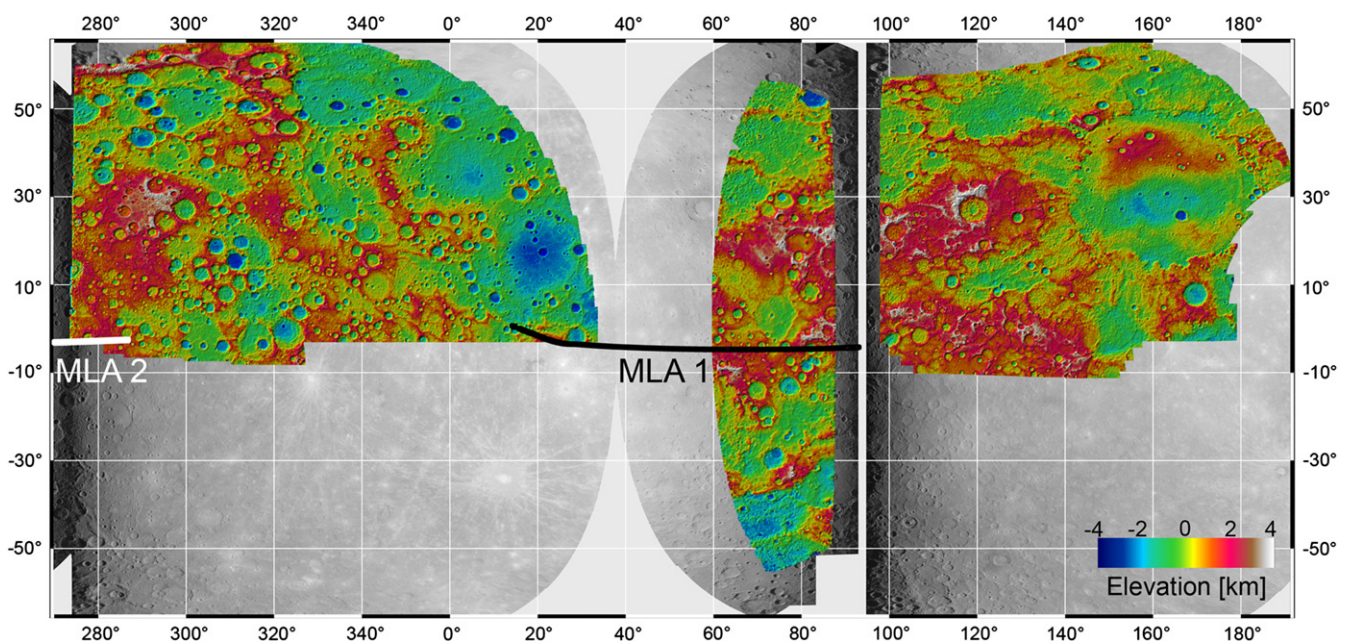

Fig. 7. Comparison of the locations of the MESSENGER stereo topographic models and the MLA profiles obtained during M1 (white) and M2 (black), overlaid on a global image mosaic.
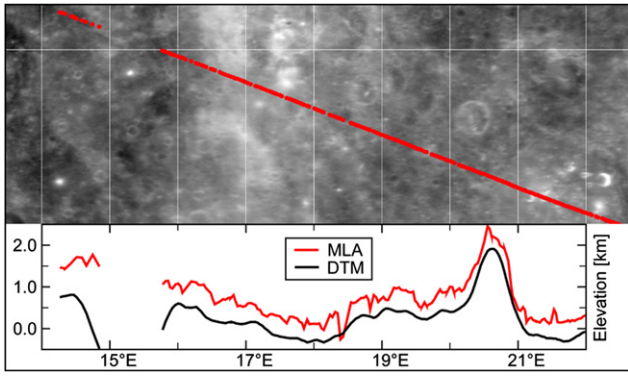
Fig. 8. Comparison of the M2 DTM with the overlapping portion of the MLA profile obtained during M1 (Fig. 7). (Top) MLA ground track plotted on the orthoimage mosaic produced with DTM. (Bottom) The MLA profile (red) and the corresponding height profile extracted from the DTM (black).
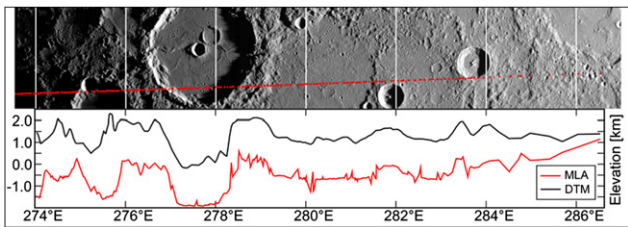

Fig. 9. Comparison of the M2 DTM with the overlapping portion of the MLA profile obtained during M2. See Fig. 8 for additional details.

over 604 km (corresponding to a mean shot spacing of 2.7 km). Unfortunately, both data sets are at their quality limits in this example. The MLA distance to the surface was 1000–1700 km, near the maximum possible range. Also, because of high incidence angles ($> 85°$) and the presence of shadows, the image data were far from optimum for stereo processing. The average range offset between the MLA profile and the M2 DTM was approximately 1400 m (Fig. 9), and both data sets are noisy near the limits of their observing periods. Note that this is the only case among our
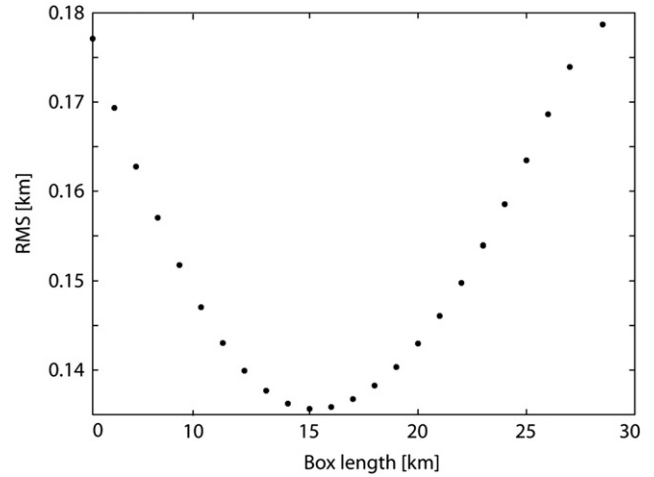

Fig. 11. RMS misfit between the M1 MLA profile and the M3 DTM plotted versus the width of the running box over which the MLA profile was smoothed by binning (see text for further explanation).
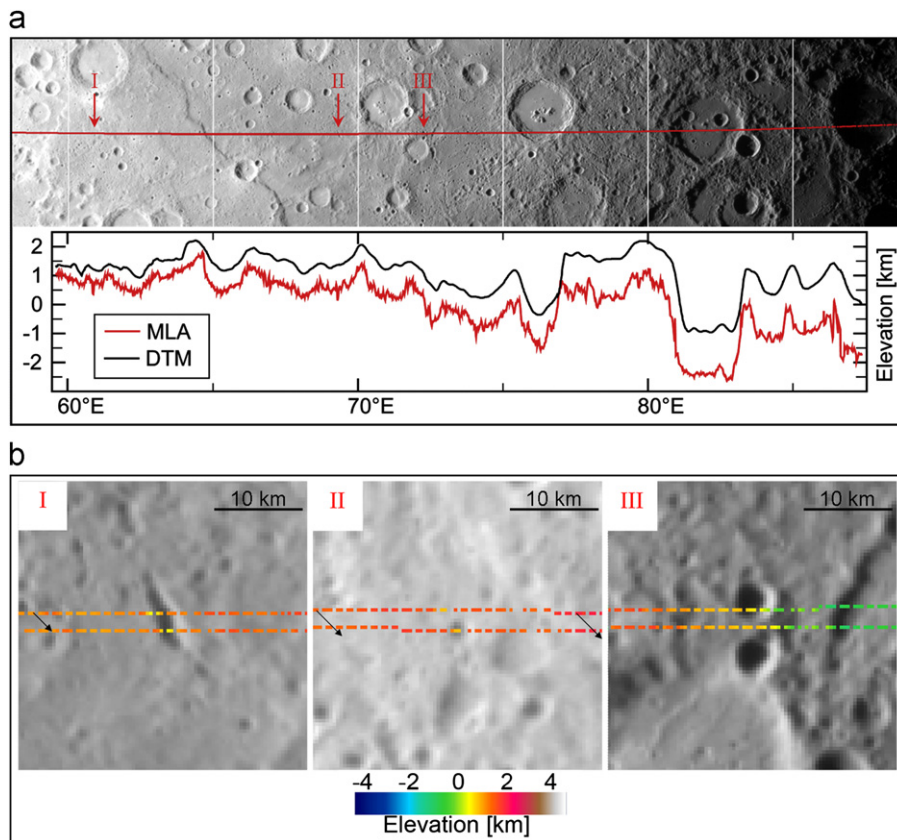

Fig. 10. (a) Comparison of the M3 DTM with the overlapping portion of the MLA profile obtained during M1. See Fig. 8 for additional details. (b) Detailed comparisons of the MLA track and the orthoimage mosaic, before and after the track has been shifted (in the direction indicated by black arrows) to best match the DTM.
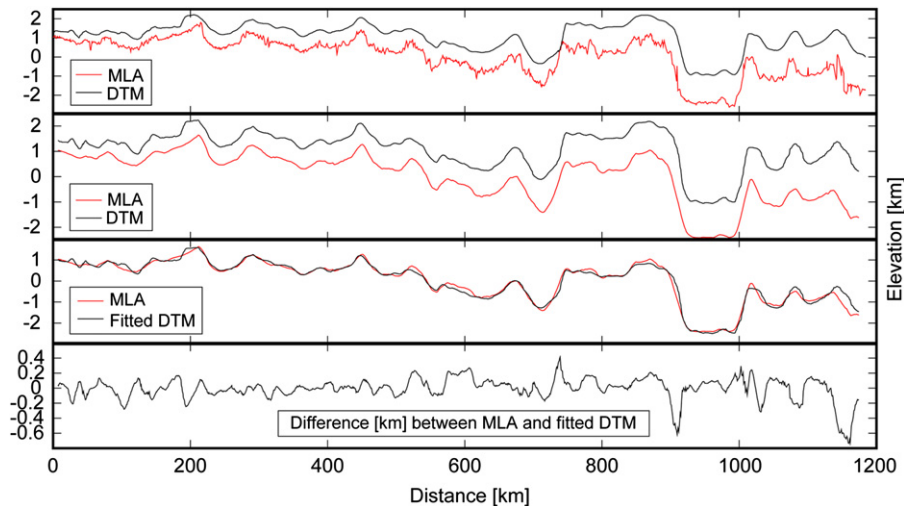
Fig. 12. Comparisons between the M1 MLA profile (red) and M3 DTM profile (black). (Top panel) Raw profiles. (Second panel) Comparison after the DTM profile has been smoothed by binning over a running box of width 15 km. (Third panel) Profiles after removal of offset and linear trend. (Bottom panel) Difference between the MLA and corrected DTM profiles (black).

three DTMs for which both data sets were obtained during the same flyby.

5.3. M3 DTM vs. MLA profile from M1

There is substantial overlap between the M3 DTM and the MLA profile obtained during M1. The overlap extends from 58° to 86°E longitude over a distance of ~1200 km, which makes it possible to compare the two topographic data sets in detail (Fig. 10a).

Although there is an overall agreement between topographic features seen in the MLA profiles and DTMs, lateral and vertical offsets between profiles from the two data sources are apparent. Root-mean-squared (RMS) height differences between the M1 MLA profile and a profile through the M3 DTM could be reduced to a minimum by shifting the MLA profile by approximately 2 km (0.05°) each in latitude and longitude (Fig. 10b) relative to the DTM. Linear regression analysis was used to determine a best-fitting linear trend in the offset between the M3 DTM and the MLA profile, which varied from 0.3 to 1.8 km from west to east. Such offsets may reflect small unmodeled pointing offsets between MDIS and MLA, errors in spacecraft trajectory knowledge, or perhaps limitations in the realization of the current Mercury-fixed coordinate system, i.e., the International Astronomical Union planetary rotation model, given that the M3 DTM was constructed from data taken during two different flybys.

From the MLA data, we made an attempt to determine the "effective resolution" of the M3 DTM. Relative height offsets and trends were first removed from the data. Next, the MLA profile was smoothed by binning within running boxes of progressively greater along-track extent to find the smoothing length that provides the best match to the corresponding profile from the DTM. On the basis of RMS residuals, best agreement between the two profiles was found when the MLA track was binned within a running 15-km-long box (Figs. 11 and 12), an indication of the "effective resolution" of the DTM. The RMS residual at best fit is 135 m. Outliers are found where slopes are steep, conditions under which DTM accuracy is affected adversely by the presence of shadows.

Hence, although the DTMs show many details of interest that are smaller than the "effective resolution" of 15 km, we suggest that quantitative measurements involving features less than 15 km in horizontal extent (e.g., measurements of the floor depths of small craters) should be treated with care. At the same time, we

note that the MLA data set may not provide a fully ideal measurement reference, as the data are discontinuous and are the product of smoothing effects on the scale of the laser spot size. Hence, our estimate of effective resolution for the DTM represents an upper limit. It should also be emphasized that the comparison applies to the particular stereo data set described here, at the given resolution, stereo angles, and illumination conditions.

6. Outlook

The stereo DTMs produced from the MESSENGER flybys will allow us to carry out a variety of morphologic studies of surface features on Mercury. The DTMs, for instance, include 400 craters larger in diameter than the effective resolution limit of 15 km, which will provide a basis for in-depth morphological study.

During its orbital mission phase, MESSENGER will obtain dedicated stereo observations under ideal illumination and viewing condition (incidence angles between 5° and 75° and low emission angles), and optimized parallax angles (approximately 20°) for global topographic models of reduced noise level and higher spatial resolution. Also, we expect that with global coverage the image blocks will be more stable and able to overcome residual height offsets and long-wavelength trend errors in the terrain models.

Moreover, MLA will obtain topographic data for the northern hemisphere as well as sparse data from the equator southwards to 20°S. These profiles, with their greater height precision, will provide absolute control and permit removal of ambiguities affecting lateral positioning and absolute heights of the stereo-derived models. Ultimately, MLA cross-track analysis will resolve remaining spacecraft orbit and instrument pointing errors, which will benefit all imaging and stereo observations. In addition, occultation measurements will provide several hundred control points for the southern hemisphere.

The currently available models constitute important tools for a variety of geological studies and will provide new insight into Mercury's surface morphology and tectonics. The models developed in this paper are available at: http://europlanet.dlr.de/MESSENGER/.

Acknowledgements

References

Cook, A.C., Robinson, M.S., 2000. Mariner 10 stereo image coverage of Mercury. J. Geophys. Res. 105, 9429–9443.

Giese, B., Oberst, J., Roatsch, T., Neukum, G., Head, J.W., Pappalardo, R.T., 1998. The local topography of Uruk Sulcus and Galileo Regio obtained from stereo images. Icarus 135, 303–316.

Giese, B., Neukum, G., Roatsch, T., Denk, T., Porco, C.C., 2006. Topographic modeling of Phoebe using Cassini images. Planet. Space Sci. 54, 1156–1166.

Gwinner, K., Scholten, F., Spiegel, M., Schmidt, R., Giese, B., Oberst, J., Jaumann, R., Heipke, C., Neukum, G., 2009. Derivation and validation of high-resolution digital terrain models from Mars Express HRSC-data. Photogramm. Eng. Remote Sensing 75, 1127–1142.

Gwinner, K., Scholten, F., Preusker, F., Elgner, S., Roatsch, T., Spiegel, M., Schmidt, R., Oberst, J., Jaumann, R., Heipke, C., 2010. Topography of Mars from global mapping by HRSC high-resolution digital terrain models and orthoimages: characteristics and performance. Earth Planet. Sci. Lett. 294, 506–519.

Hawkins III, S.E., Boldt, J.D., Darlington, D.H., Espiritu, R., Gold, R.E., Gotwols, B., Grey, M.P., Hash, C.D., Hayes, J.R., Jaskulek, S.E., Kardian Jr., C.J., Keller, M.R., Malaret, E.R., Murchie, S.L., Murphy, P.K., Peacock, K., Prockter, L.M., Reiter, R.A., Robinson, M.S., Schaefer, E.D., Shelton, R.G., Sterner II, R.E., Taylor, H.W., Watters, T.R., Williams, B.D., 2007. The Mercury Dual Imaging System on the MESSENGER spacecraft. Space Sci. Rev. 131, 247–338.

Hawkins III, S.E., Murchie, S.L., Becker, K.J., Selby, C.M., Turner, F.S., Nobel, M.W., Chabot, N.L., Choo, T.H., Darlington, E.H., Denevi, B.W., Domingue, D.L., Ernst, C.M., Holsclaw, G.M., Laslo, N.R., McClintock, W.E., Prockter, L.M., Robinson, M.S., Solomon, S.C., Sterner II, R.E., 2009. In-flight performance of MESSEN-GER's Mercury Dual Imaging System. In: Hoover, R.B., Levin, G.V., Rozanov, A.Y., Retherford, K.D. (Eds.), Instruments and Methods for Astrobiology and Planetary Missions. SPIE Proceedings, vol. 7441. SPIE, Bellingham, Wash, pp. 12 (paper 7441A-3).

Oberst, J., Preusker, F., Phillips, R.J., Watters, T.R., Head, J.W., Zuber, M.T., Solomon, S.C., 2010. The morphology of Mercury's Caloris basin as seen in MESSENGER stereo topographic models. Icarus 209, 230–238.

Scholten, F., Gwinner, K., Roatsch, T., Matz, K.-D., Wählisch, M., Giese, B., Oberst, J., Jaumann, R., Neukum, G., Team, Co-Investigator, 2005. Mars Express HRSC data processing—methods and operational aspects. Photogramm. Eng. Remote Sensing 71, 1143–1152.

Slade, M.A., Jurgens, R.F., Rojas, F., 1997. New radar topography of Mercury and the need for a Mercury DTM. Lunar Planet. Sci. 28 (abstract 1333).

Smith, D.E., Zuber, M.T., Phillips, R.J., Solomon, S.C., Neumann, G.A., Lemoine, F.G., Peale, S.J., Margot, J.-L., Torrence, M.H., Talpe, M.J., Head III, J.W., Hauck II, S.A., Johnson, C.L., Perry, M.E., Barnouin, O.S., McNutt Jr., R.L., Oberst, J., 2010. The equatorial shape and gravity field of Mercury from MESSENGER flybys 1 and 2. Icarus 209, 88–100.

Solomon, S.C., McNutt Jr., R.L., Watters, T.R., Lawrence, D.J., Feldman, W.C., Head, J.W., Krimigis, S.M., Murchie, S.L., Phillips, R.J., Slavin, J.A., Zuber, M.T., 2008. Return to Mercury: a global perspective on MESSENGER's first Mercury flyby. Science 321, 59–62.

Watters, T.R., Cook, A.C., Robinson, M.S., 2001. Large-scale lobate scarps in the southern hemisphere of Mercury. Planet. Space Sci. 49, 1523–1530.

Watters, T.R., Solomon, S.C., Robinson, M.S., Head, J.W., André, S.L., Hauck II, S.A., Murchie, S.L., 2009a. The tectonics of Mercury: the view after MESSENGER's first flyby. Earth Planet. Sci. Lett. 285, 283–296.

Watters, T.R., Head, J.W., Solomon, S.C., Robinson, M.S., Chapman, C.R., Denevi, B.W., Fassett, C.I., Murchie, S.L., Strom, R.G., 2009b. Evolution of the Rembrandt impact basin on Mercury. Science 324, 618–621.

Wewel, F., 1996. Determination of conjugate points of stereoscopic three line scanner data of Mars 96 mission. Int. Arch. Photogramm. Remote Sensing 31, 936–939.

Zuber, M.T., Smith, D.E., Solomon, S.C., Phillips, R.J., Peale, S.J., Head III, J.W., Hauck II, S.A., McNutt Jr., R.L., Oberst, J., Neumann, G.A., Lemoine, F.G., Sun, X., Barnouin-Jha, O., Harmon, J.K., 2008. Laser altimeter observations from MESSENGER's first Mercury flyby. Science 321, 77–79.